RESEARCH

Check for updates

Wavepacket Modelling of Jet-Flap Interaction Noise: from Laboratory to Full-Scale Aircraft

Jérôme Huber[1] · Grégoire Pont[2] · Peter Jordan[3] · Michel Roger[4]

Abstract

Purpose A key component of aircraft acoustic installation effects relevant for under-wing turbofan-powered airliners, is studied: jet-flap interaction noise.

Observations First, noise measurements performed on laboratory jets and on realistic engine exhaust geometries are analyzed to gain understanding both on surface pressure in the jet near-field and on far-field acoustics. The analysis of experimental datasets at various scales underlines intense, advecting, coherent and exponentially-growing pressure signatures in the jet near field and on the wing under-side. The outcome confirms our hypothesis for the main mechanism driving jet-flap interaction noise: coherent organized turbulent structures.

Methods Relevant physical models are selected and chained together. RANS CFD and stability analysis model the characteristics of jet wavepackets as noise sources, analytical tailored Green's functions and Boundary Element Method (BEM) predict the diffraction of the wavepackets by the airframe.

Results For academic configurations where a flat plate models the wing and flap, the wavepacket model is found able to capture noise directivity and trends. The significant impact of a swept trailing edge and the contributions of other plate edges lead us to design, test and simulate a plate with realistic wing plan form. The wavepacket-BEM simulation reproduces jet-surface interaction for the wing plan-form plate, as well as jet-flap interaction on realistic models tested at ONERA CEPRA19 facility during large-scale wind-tunnel tests. Wing-mounted unsteady pressure sensors are utilized as first control points. Then, polar and azimuthal acoustic directivity is examined. Discrepancies between experiments and simulations are identified. Finally an installation geometrical effect is computed: the vertical separation H between nozzle and wing is varied to replicate the tests.

Conclusion The diffraction of coherent organized turbulent structures generates jet-flap interaction noise in the academic jet laboratory, in large-scale wind-tunnel test and on the full-scale aircraft. We conclude on the potential and the limits of the proposed wavepacket-BEM model to predict the sound field, and we outline the perspectives for future modelling and testing.

Keywords Wavepackets · Jet-flap interaction noise · Stability analysis · BEM

Extended author information available on the last page of the article

List of Symbols

a_0	Ambient speed of sound (m/s)
α	Eigenvalue of local stability problem
C	Wing chord (m)
D	Nozzle jet diameter (m)
$D_{p/s/m}$	Primary/secondary/fully-mixed jet diameter (m)
ϵ	Wing thickness (m)
f	Frequency (Hz)
H	Radial separation between jet and flap trailing edge (m)
JFI	Jet Flap interaction
k_a	Acoustic wavenumber (m)
k_h	Axial convective or hydrodynamic wavenumber (m)
L	Axial separation between jet and flap trailing edge (m)
λ_a	Acoustic wavelength (m)
λ_h	Wavepacket hydrodynamic wavelength (m)
M, M_j	Jet Mach number
$M_{a,j}$	Jet acoustic Mach number, $M_{a,j} = \dfrac{U_j}{a_0}$
M_c	Convection Mach number
M_f, M_0	Flight Mach number
ν	Kinematic viscosity (m²/s)
ω	Angular frequency (rad/s)
ϕ	Azimuthal angle, see Fig. 5(a)
PSD	Power Spectral Density
PSE	Parabolized Stability Equations
ρ	Density (kg/m³)
ρ_0	Reference density in medium (kg/m³)
Re	Reynolds number, Re$= \dfrac{UD}{\nu}$
St	Strouhal number, $St = \dfrac{fU}{D}$
$T_{s,j}$	Static jet temperature (K)
$T_{t,j}$	Total jet temperature (K)
T_0	Static ambient temperature (K)
$t+$	Convective time $t+ = \dfrac{tU_j}{D_j}$
TE	Trailing edge
θ	Polar angle, 0 points downstream, see Fig. 5(a) (°)
U, U_j	Jet mean velocity (m/s)
U_c, U_ϕ	Convection or phase velocity (m/s)
$U_{p/s/m}$	Primary/secondary/fully-mixed mean jet velocity (m/s)
x	Observer position
y	Source position

Reference System

This study uses the coordinate system presented in Fig. 5, from Piantanida et al. (2016). The polar angle θ is relative to the jet axis with 0° pointing downstream. The azimuth angle Φ is set to 0° in the spanwise direction of the wing on the starboard side of the aircraft.

1 Introduction

Understanding and predicting jet-flap interaction noise is the main focus of this work. Part of *Propulsion-Airframe Aeroacoustics* (PAA), jet-flap interaction (JFI) noise is a component of *installed jet noise*, the term used here to describe the total noise due to an engine jet installed on an airframe. Figure 1 illustrates key parameters to consider for JFI noise in the case of a jet engine installed under wing. The engine integration is here described using the nozzle and jet diameters D_m, and the installation geometry with distances H and L. Installed jet flow dynamics include features such as jet redirection by the wing and passage under the flap at an effective radial distance H_{eff}.

We refer to *installation effects* as the difference in sound pressure level between installed and isolated nozzle configurations. A separation of aeroacoustic installation effects into source and propagation mechanisms is proposed. Three *source* mechanisms are envisaged as (1) jet noise sources responsible for direct sound radiation may be modified due to the mean flow deformation caused by installation; (2) jet-surface interaction (JSI) noise, of which the main component is jet-flap interaction (JFI) noise. Jet-flap interaction is due to jet near field scattering by the lifting wing as the jet flow passes close to the surface and particularly to the trailing edge. This interaction creates broadband noise; (3) jet-flap impingement is expected to create broadband noise and possibly tonal noise via resonances. Additionally two *propagation* mechanisms are expected to influence the installed jet far-field signature: (1) jet-surface reflection of acoustic waves is expected to increase noise particularly at medium and high frequencies, (2) jet acoustic blockage shields the flyover observers from reflected waves and redirects energy to lateral directions.

Jet installation noise has been studied extensively since the 1970s, with numerous reports of measured noise directivity and trends at different scales and complexity levels. However modelling attempts of the noise generation mechanisms are mostly recent and fewer in number.

Jet-flap interaction noise has been identified in dedicated flight tests, first on a DC-10 as reported by Low (1977) and later on a 707 CFM56 by SenGupta (1983). On the DC-10, Low identified the noise source in the frequency range [50, 250] Hz, typically $St \in$ [0.2, 1]. A significant noise increase was measured when the jet impinged on the flap at approach conditions, at which the flap is deflected at an angle greater than 30°.

In the 1970s Head and Fisher Head and Fisher (1976) reported on lab tests performed with a single-stream jet and flat plate. Scattering of the jet near field at the wing trailing edge (TE) was recognized even when the jet was not "*ostensibly interacting with*" the plate. They concluded that a jet-plate interaction noise source could be modelled as a dipole perpendicular to the plate, located at the trailing edge and suggested it was driven by local near-field *acoustic* pressures. Similar experiments and conclusions repeated in the recent

Fig. 1 Problem definition of the installed co-axial jet, including the main parameters used in this work. The sketch uses an earlier work by Lawrence (2014)
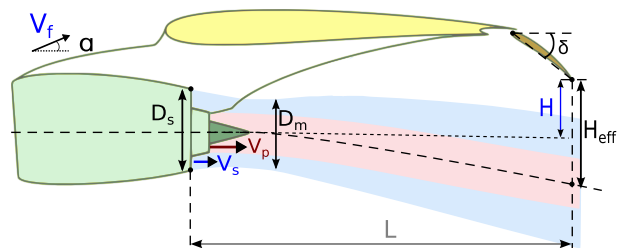
years with Cavalieri et al. (2014) and Piantanida et al. (2016), except for the near-field pressure was now proved to be non acoustic but hydrodynamic.

In the early 1980s numerous studies focused on scaled-model experiments in wind tunnels. A main motivation was to explain the noise gaps identified between full-scale aircraft hence an installed propulsion system, and scaled models of engine exhausts tested in simulated flight conditions but isolated. A number of reports e.g. Bushell (1975); Reddy (1980); Southern (1980); Way and Turner (1980) and Wang (1980) showed that installation effects cause low-frequency amplifications that explain part of the noise measured in aircraft flight tests. SenGupta (1983) and Miller (1983) studied installed scaled models including a realistic 1:13-scale B757 model in the Boeing company wind-tunnel. SenGupta suggested that the noise amplification due to installation was due to lift fluctuations at low frequency, trailing-edge diffraction at mid frequency and jet noise reflection at high frequency. A significant contribution of Miller (1983) is the identified role of the wing leading edge in the diffraction process. The ratio between wing chord and acoustic wavelength C/λ_a drives the multi-lobe directivity shape. Miller proposed an empirical model for JSI polar directivity to account for the interference between two acoustic waves originating from the trailing edge and travelling upstream, one above and the other below the wing. Lawrence (2014) recently corroborated Miller's model with flat plate laboratory data in static conditions. Shearin (1983) and Brown and Ahuja (1984) identified the influence of various airframe geometrical features and installation parameters on total noise. Noise increases when (i) vertical separation H is lowered, (ii) axial separation L is increased, (iii) flap deflection δ is increased (reducing H), (iv) flap cut-out width is decreased, and when (v) jet velocity is increased. Shivashankara and Blackner (1997) published an extensive reduced-scale model test representing a large airplane, at the LSAF wind-tunnel facility [16],Viswanathan (2010). Source imaging confirmed the importance of the flap trailing edge downstream of the engine.

In the 2000 s, Elkoby (2005) studied installed jet noise at full scale by comparing flight tests measurements and engine data projected to flight without installation effects. Noise increases at take-off turned out to be similar to wind-tunnel results, yet the source mechanisms were not inferred. Mengle et al. (2006a, 2006b, 2007); Mengle (2011) used an out-of-flow source location technique in large-model-scale tests to interpret the effect of chevron and flaperon designs on jet-flap interaction noise. Asymmetric chevrons with enhanced mixing near the pylon were found more effective at reducing JFI noise than symmetric chevrons. Jet flow distortion under wing and the effectiveness of serrations at reducing JFI were experimentally quantified in large-scale wind-tunnel tests at ONERA CEPRA19 Piccin (2009) and reported by Davy et al. (2009); Dezitter et al. (2009) and Huber et al. (2009). Subsequent investigations at CEPRA19 reported by Huber et al. (2014); David et al. (2014) and Fleury and Davy (2014) confirmed the three-source view formulated above. The jet was found to dominate the unsteady fluctuating pressure in measurements on the wing and flap underside. The data demonstrated the organisation and the exponential growth of unsteady wall pressure in the streamwise direction even in complex geometries with pylon. Meloni et al. (2020) analysed unsteady wall pressure measurements at CEPRA19 in both static and flight conditions and confirmed wavepacket signatures on the wing model.

Perrino (2014) characterized experimentally at laboratory scale a number of realistic geometry effects including engine-wing position and flap deflection. Belyaev et al.[32] studied realistic configurations at small scale as well in a TsAGI wind tunnel and demonstrated the exponential amplification of noise with flap deflection, reinforcing the motivation for modelling jet-flap interaction noise sources using coherent structures. Bychkov and Faranosov (2014, 2018) proposed a procedure to compute jet near-field scattering using

the Wiener-Hopf technique. Bychkov et al.[35] use PSE on measured mean flow to represent the near-field pulsations as wavepackets. Not only the model reproduces the effect of flight on an acoustic spectrum in the range $St \in [0.3, 0.8]$, but once calibrated it is also capable of predicting correctly the absolute levels within a few dB. The philosophy of the source modelling is similar to our present work, and provides interesting perspectives for our modelling of jet installation noise in flight.

Lyu et al. (2017); Lyu and Dowling (2017) elaborated a two-fold strategy toward a fast-return prediction of installed jet noise: a scheme for low-frequency amplification and another for high-frequency reflections. To tackle the diffraction of hydrodynamic instabilities, Lyu and Dowling decomposed a given evanescent near-field pressure into a series of plane waves and derived the scattered field using Schwarzschild's technique. The source terms require information from either experiments or high-fidelity simulation, as no instability source modelling is proposed. Lyu and Dowling used the model to study swept wings as a noise reduction technology Lyu and Dowling (2019) and found similar conclusions as Piantanida et al. (2016). Dawson et al. (2020) decomposed in-flight near-field pressure measurements to validate the works of Lyu et al. (2017), and obtained satisfactory agreement in static and up to flight Mach number $M_f = 0.2$.

Our objective is two-fold. Our first aim is to establish the importance of organized turbulence structures for jet-flap interaction noise across a wide range of scales all the way to the commercial aircraft, through both published and novel experiments. Our second objective is to assess how a simplified physics-based modelling approach may characterize JFI noise for various designs and levels of complexity, including realistic geometries.

The remainder of this paper is organized as follows. In 2 we present the different experimental setups and a data analysis for the near-field and the far-field pressure. We propose a simplified modelling methodology in 3 and assess it against tested cases of increasing complexity levels in 4. Some concluding notes are proposed in 5.

2 Jet Installation Noise Measurements

This section presents noise measurements performed at different scales: full-scale experiments on an aircraft in flyover, realistic wind-tunnel tests, and jet laboratory tests on a canonical jet plate configuration. First, each test is described. In a second step, the free-field measurements are presented. Pressure data recorded in the source near field is analyzed next. Finally conclusions and perspectives for noise source modelling are proposed.

2.1 Tests Description

Full-scale flyover tests are presented first. Then the jet installation problem is replicated at a reduced scale in a large anechoic wind tunnel. At last the problem is further simplified into a canonical configuration: laboratory tests are conducted with flat plates interacting with a single-stream nozzle jet.

2.1.1 Flight Tests

This section presents acoustic measurements performed by Airbus during two flight test campaigns on widebody A350 aircraft. This twin-jet airliner is equipped with a Rolls-Royce Trent XWB engine[40] of ByPass Ratio around 10. A first test campaign focused

on jet-flap interaction noise characterization in the *far field* with ground microphones and source localization array. The second campaign characterized the *near-field* wall pressure fluctuations on the wing pressure side of the same aircraft model.

Flyover noise tests and instrumentation are illustrated in Fig. 2. For the far-field noise measurements during flyovers, ground microphones are placed on specific plates of large scale to mitigate ground effects and with a daisy design to reduce edge diffraction Blandeau et al. (2018); Blandeau and Bousquet (2021); Blandeau et al. (2023). A cross-shaped source-localisation array is installed at ground level, with its center positioned under the flyover path. A total of 249 microphones are arranged over 74-meter segments in sub-arrays to cover a wide range of frequencies. Additional details on the array design can be found in Leiba et al.[44].

Each flyover is used to characterize installed jet noise for a given high-lift-device configuration, a flight Mach number and an engine setting. Both engines are set to the same regime. The pilots stabilize the aircraft at these parameters over a range of polar angles. On this specific flight test, stabilization at upstream polar angles is given particular care so as to study jet-flap interaction noise. The passage altitude above the source-localisation array, of the order of 200 m, allows for a separation of the different noise sources.

A first analysis of the flight parameters ensures that the aircraft Mach number, the angle of attack and the engine rotation speed remain stable through the acoustic-measurement phase of the flyover. The angle of attack is representative of take-off. Engine settings translate into nozzle pressure ratios through an engine performance table, and further into mean exhaust Mach numbers. The reproduction of the altitude, flight Mach number and engine settings across flyovers is such that the jet Mach numbers and the flight Mach number display small dispersion around the specified values. The dispersion envelope of the Mach difference to the power eight shows a maximum of 1 dB SPL, as shown in Eq. 1.

$$\max^{i}[80 \, log_{10}(M_j^i - M_f^i)] - \min^{k}[80 \, log_{10}(M_j^k - M_f^k)] \le 1 \text{ dB SPL}, \tag{1}$$

where indices i and k sweep across the repeat flyovers. The result stands regardless of whether the jet Mach number M_j represents the secondary jet or the fully-mixed jet. The variation for an exponent five, expected for jet-flap interaction noise, is less than 1 dB SPL. This dispersion between individual flyovers remains well below the magnitude of the noise amplification through flap deflection, studied in Sect. 2.2.1.
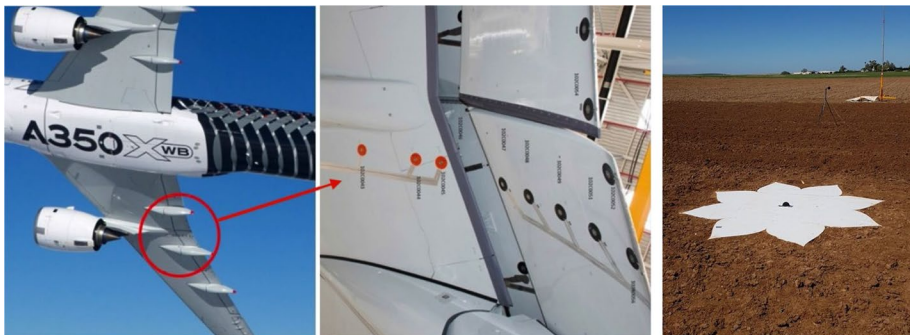

Fig. 2 A350 aircraft, on-board instrumentation and ground microphone on daisy plate. The on-board microphones are flush-mounted at the center of round elastomer pads, of red color on the main wing and black on the flaps. Pictures are Airbus copyright

Studying low-frequency aeroacoustic sources in flight test is not a trivial task, partly because the aircraft spends a limited time within a few degrees of a given polar angle. Signal time at the polar angle of interest may not be large compared to the time scale of the source events in the flow. However, thanks to the multiple daisy-plate microphones and the repeatability of the noise-driving flight parameters, the conclusions drawn on individual flyovers are statistically confirmed.

The near-field test campaign aimed at measuring the unsteady surface pressure under wing in conditions replicating the far-field tests. Thirteen microphones were installed on the pressure side of the right hand-side wing, downstream from the engine as shown in Fig. 2. These microphones can be grouped into a streamwise array and a spanwise array. The streamwise set is located on an axis parallel to the engine axis 0.3 D_m outwards of the pylon symmetry plane, includes three microphones on the wing and five microphones on the flap. The spanwise set of sensors is located along the trailing edge of the flaps.

2.1.2 Wind-Tunnel Tests

A series of wind-tunnel tests performed by ONERA at the CEPRA19 facility Piccin (2009) are used. The two tests EXEJET and AMBROSIA were performed in the frame of a partnership between Airbus and Safran Aero Engines. The JERONIMO test was in the frame of a partnership between Airbus, Rolls-Royce Deutschland, Safran Aero Engines and ONERA. These large-scale jet noise tests use realistic geometries and flow conditions, and allow exploring the aeroacoustic phenomena at play at full scale [45]. The CEPRA19 tunnel convergent delivers a two-meter diameter co-flow stream that replicates the aircraft flight condition at any specified Mach number up to 0.3. The nozzle models are dual-stream coaxial geometries, have a typical nozzle diameter of 20 cm, and can be used either with a pylon model or in an axisymmetric configuration. The Airbus REX80 wing model was designed specifically for this wind tunnel. The wing chord at the powerplant station is in the range $D_m \in [2, 3]$ pending on nozzle model and conditions in those tests. The wing TE is at a sweep angle of 7°. Figure 3 reveals the JERONIMO nozzle and the REX80 wing model installed in the CEPRA19 test chamber. Additional details on the test set-up and on the wing model may be found in Huber et al. (2014).

Fig. 3 Axisymmetric nozzle and REX80 wing model in CEPRA19, Onera. JERONIMO test campaign. Airbus ONERA Rolls-Royce Safran collaboration

During the AMBROSIA wind-tunnel tests, model configurations simulated various nozzle-to-wing distances, thus allowing to study the influence of the installation geometry on jet-flap interaction noise. Installed configurations were tested over a significant range of H/D values by translating the wing model up and down relatively to the axisymmetric nozzle model. A model deformation measurement system by ONERA based on triangulation provided the nozzle and wing positions in test chamber in real time. The H values achieved could therefore be assessed with high accuracy.

While CEPRA19 has the capability to generate realistic heated dual-stream engine jets, matched-jets conditions were also achieved to effectively create a dual-stream jet flow similar to a single stream. At matched-jets condition, the Mach numbers for the primary jet (j, p) and secondary jet (j, s) are equal, $M_{j,p} = M_{j,s}$, and so are the static temperatures $T_{j,p} = T_{j,s} \simeq T_0$. Noise data was acquired with the 2-meter flight stream, and also at static ambient conditions by turning off the flight stream.

2.1.3 Simplification of the Problem

Studying jet-flap interaction noise on a canonical geometry implies conserving the physics at play at larger scale. The use of a reference single-stream jet and flat plates to simulate the wing and flaps has been done repeatedly. This degree of simplification turns out to be adapted to our study focused on high-bypass ratio turbofans. For these engines, the mass flow in the secondary duct is about ten times higher than in the core. The secondary jet velocity is expected to drive the most intense near-field fluctuations, although caution must be taken as the primary jet may drive a downstream part of the near field when primary jet velocities are high, as reported Léon and Brazier (2013). The dual-stream jet is therefore simplified with a single-stream jet of diameter $D = D_m$ and $U = U_s \simeq U_m$.

A dimensional analysis can conclude on the main parameters driving jet-flap interaction noise: Eq. 2 presents flow and geometrical variables at play. In terms of installation geometry, the engine exhaust is typically close to the wing leading edge therefore the axial separation is about equal to the wing chord, $L \simeq C$. Typical axial separation distances L for modern commercial aircraft are in the range $[2D_m, 6D_m]$. The engine is installed at a vertical distance H from the flap edge, and the wing lift modifies the vertical separation to an effective H_{eff}. Steady CFD is expected to be able to provide H_{eff} hence this parameter can replace both H and lift coefficient C_L. Wing are typically thin in the sense that $\epsilon \ll C$ therefore $\epsilon < \lambda_a$. Wing thickness may therefore be neglected and Lawrence (2014) and Piantanida (2017) have confirmed this hypothesis experimentally. The wing-flap gap distance is also very small compared to λ_a. Finally, wing camber is neglected despite the flap deflection δ, moderate on take-off configurations, to propose a flat plate representation of the wing. The parameters in Eq. 2 is therefore reduced to two velocities and three characteristic lengths in Eq. 3.

$$SPL = f(U_p, U_s, U_f, D_m, H, L, C, C_L, \delta, \epsilon, \text{planform}), \tag{2}$$

$$\simeq f(U_s, U_f, D_m, H_{\text{eff}}, L, \text{planform}). \tag{3}$$

These reduced parameters justify that a flat plate interacting with a single-stream jet may be used to gain understanding on jet-flap interaction aeroacoustics. Various vertical separations H and two plate planforms are studied next.
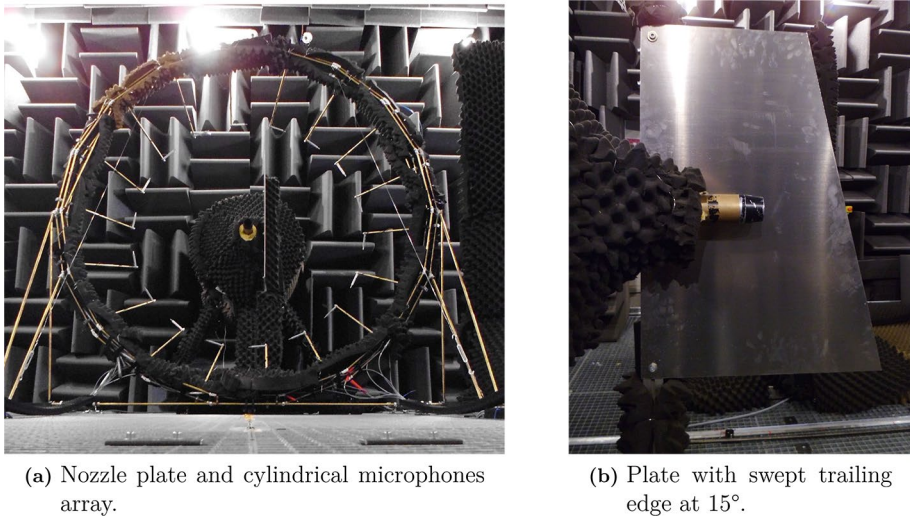
(a) Nozzle plate and cylindrical microphones array.

(b) Plate with swept trailing edge at 15°.

Fig. 4 Jet-plate experiment at Bruit et Vent, PPRIME, by Piantanida and Jaunet. Pictures are Airbus and PPRIME copyright
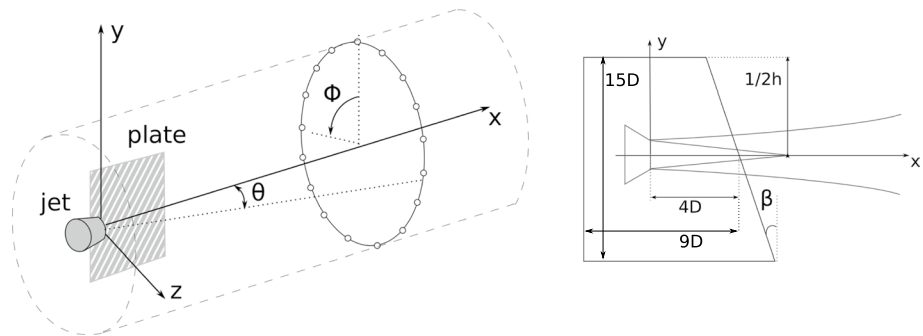

Fig. 5 Sketch of the experimental layout: jet-plate system, measurement surface and coordinate system conventions (left), plate characteristics and position (right). From Piantanida et al. (2016)

2.1.4 Jet Laboratory Tests

The experiments were performed in the *Bruit et Vent* anechoic facility of the PPRIME Institute, Poitiers, France. The anechoic chamber has dimensions of 9.6 m × 6 m × 3.4 m, and is equipped with absorbing foam of depth 0.4 m. The cut-off frequency is 212 Hz. The nozzle of diameter $D = 0.05$ m was used in a number of investigations Cavalieri et al. (2012a); Breakey (2013); Cavalieri et al. (2014) where the flow and sound fields have been extensively studied in an uninstalled configuration. The acoustic Mach number, defined as $M = U/a_0$, with U the mean jet velocity at nozzle exhaust and a_0 the ambient speed of sound, was varied in the range $0.4 \leq M \leq 0.9$. The jet was isothermal, $T_{sj}/T_0 = 1$, and a boundary layer trip placed $2.7D$ upstream of the nozzle lip ensured a fully turbulent boundary layer at the jet exit.

Flat aluminum plates with varying trailing-edge sweep angle were mounted with their flat surface parallel to the jet. Plates spanned $15D$ and the mid-span chord was fixed at $9D$. The plate thickness was $0.06D$. The plate leading edge was clamped to a support that allows the plate to be moved in the radial direction, with respect to the jet axis. The mid-span of trailing edge is situated at $L/D = 4$ from the nozzle exhaust plane in the jet flow direction as illustrated in Fig. 5. For each sweep angle β, the radial position of the plate and the jet Mach number were varied in order to explore the effect of each parameter on the sound field. Parameters space covered the sweep angle range $0° \leq \beta \leq 45°$, Mach number range $0.4 \leq M \leq 0.9$ and jet-plate radial distance range $0.6 \leq H/D \leq 2$ from the jet center line.

The minor effect of the plate on the jet mean flow for distances $H/D \geq 1$ was verified experimentally by Cavalieri et al. (2012b) and our RANS CFD on the same jet-plate cases confirmed this fact.

Piantanida and Jaunet performed extensive acoustic measurements using an 18-microphone azimuthal array of radius $r/D = 14.3$ hence in the geometrical near field. The sound field was mapped on a cylindrical surface surrounding the jet-plate system. Figure 4 presents two pictures of the experimental setup: Fig. 4(a) shows the microphone measurement array traversing around the models. Figure 4(b) illustrates the plate and the nozzle location. Additional details on the experimental setup may be found in Piantanida et al. (2016).

A sketch of the experimental layout is provided in Fig. 5, including the reference coordinate system, the polar (θ) and azimuthal (ϕ) angle conventions used.

2.2 Analysis of Far-Field Measurements

Aircraft flyover test data is presented first. An analysis of wind-tunnel test data follows, and a comparison of datasets concludes with a broad range of model scales.

2.2.1 Flight Test Results

For a typical take-off engine power condition, a measurable noise level increase in the forward arc was identified when the flap is deflected toward the jet, similarly to previous flight tests with DC-10 and B707 Low (1977); SenGupta (1983). Figure 6 presents two spectra associated with distinct flap deployments, all other relevant flight parameters being

Fig. 6 Acoustic narrowband pressure spectra measured at $\theta = 130°$ for two flap deflections. Takeoff engine power condition. A350 flight test campaign. Airbus copyright
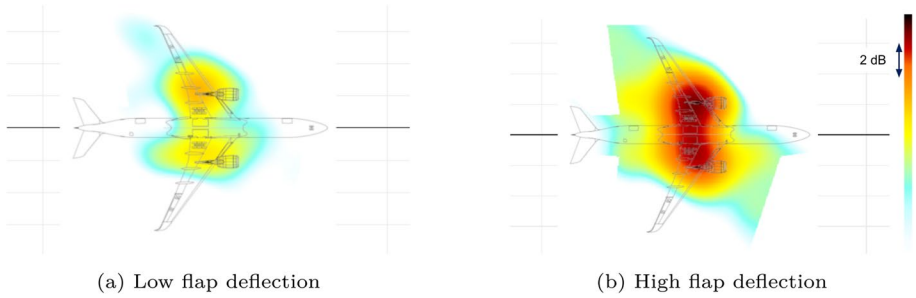
(a) Low flap deflection   (b) High flap deflection
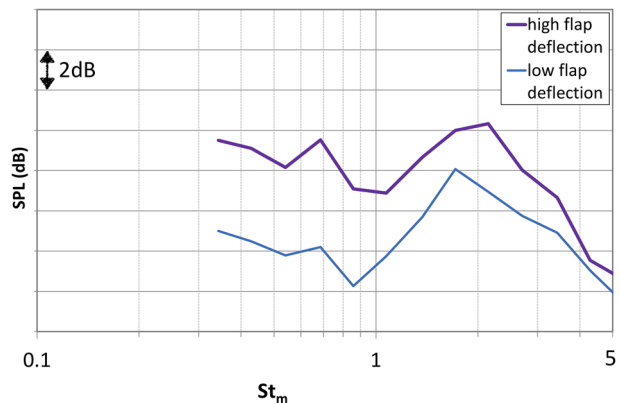
Fig. 7 Noise source maps for two flap deflections corresponding to measurements at $\theta = 100°$ in the upstream direction, at $St_m = 0.9$. Both maps share the same pressure level scale. Take-off engine power condition. A350 flight test campaign. Airbus copyright

Fig. 8 Acoustic narrowband pressure spectra measured near the peak of installation noise in CEPRA19 at $\theta = 130°$ for different vertical distances H/D. Unheated matched jets at $M_j = 0.6$ in static conditions. AMBROSIA test campaign
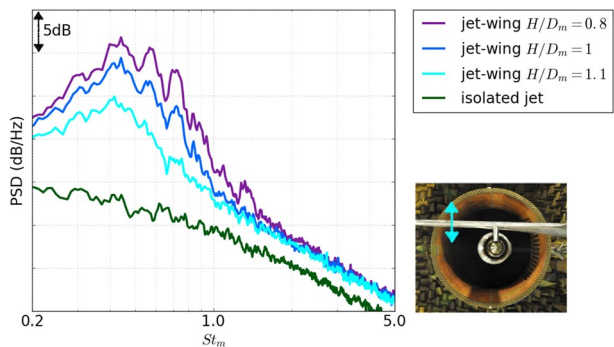
reproduced. The noise increase of 4 to 5 dB in the frequency range $St_m \in [0.3, 1]$ is attributed to jet-flap interaction noise. The noise levels also increase at higher frequency $St_m > 1$, with other installation effects being possible contributors.

The ground-based source-localisation array supports this conclusion. The data processing presented here is performed following Fleury and Bulté (2011). Figure 7 shows two noise-source maps corresponding to the two flap configurations for which spectra are presented in Fig. 6. The noise maps share the same color scale. While having limited capability at low frequency, the array technique focused on $St_m = 0.9$ reveals source activity near the flap on the low-flap-angle case. This source becomes more intense with increased flap deflection, with a sound pressure level increase at the flap location around 5 dB, the same magnitude as on the autospectra in Fig. 6.

2.2.2 Wind-Tunnel Test Results

Free-field noise spectra for installed and uninstalled nozzles measured by a forward-arc microphone are presented in Fig. 8. The distance between the REX80 wing and the axisymmetric nozzle was varied in the range $H/D_m \in [0.8, 1.1]$. The sound amplification up to 15 dB observed at $St_m \in [0.2, 1.5]$ increases with a reduced radial distance H/D_m. The frequency range at which the amplification occurs above 3 dB increases with decreasing H distance. This amplification is attributed to jet-flap interaction noise. The noise increase in the frequency range $St_m \in [1.5, 5]$ lies between 2 to 3 dB and is attributed to jet noise
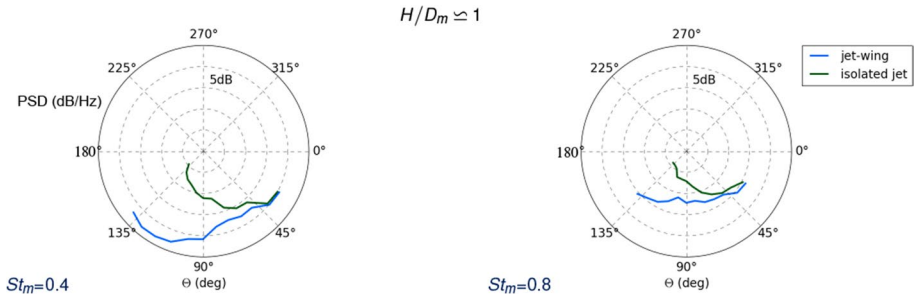
Fig. 9 Polar directivity of sound pressure levels measured in CEPRA19 in flyover direction for a $H/D_m \simeq 1$ configuration with axisymmetric nozzle and REX80 wing model. $M_j = 0.6$, unheated matched jets in static conditions. AMBROSIA test campaign
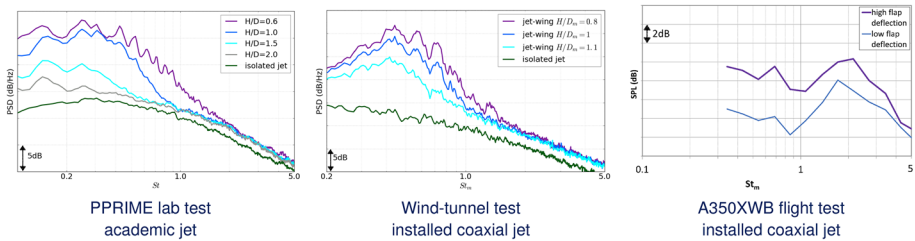

Fig. 10 Jet installation noise measured at different scales

reflection by the wing. The array analysis reported by Fleury and Davy (2014) confirmed this scenario, with strong source activity identified near the flap trailing edge at $St_m = 1$, and source activity in the jet plume and reflected sound image at $St_m \geq 2$.

Figure 9 presents the sound directivity of two frequencies for a model configuration tested in wind tunnel, where $H/D_m \simeq 1$. While the isolated nozzle jet displays the classical aft directivity of direct jet noise with a dynamic of 10 to 15 dB, jet-flap interaction noise dominates the installed jet signature in the forward arc with a 10 to 20 dB amplification. Jet-flap interaction noise appears to have a marked forward-arc directivity at most frequencies. Overall, the CEPRA19 measurements used in this study confirm the broadband noise amplification shown in previous publications, for instance Mead and Strange (1998); Mengle (2011); Cavalieri et al. (2014).

A comparison between this large-scale data, the flight test data and jet laboratory tests results is proposed next.

2.2.3 Comparison of Measurements from the Different Scale Experiments

Figure 10 confirms the qualitative similarity of far-field noise signature for jet-plate interaction and for jet-flap interactions in wind tunnel and in flight. The free-field noise measurements confirm trends observed on conventional jet-airframe interaction in previous publications Mengle et al. (2006b); Huber et al. (2009); Mengle (2011). Conventional jet-airframe interaction noise tends to dominate at low Strouhal numbers $St_m \in [0.3, 1.5]$ and forward polar angles. The noise amplification at frequencies below $St_m = 0.4$ differs between the lab case and the wind-tunnel test. The difference can be largely explained by

the different positions of the trailing edges with respect to the jet: low-frequency wavepackets have a relatively low energy when they cross the flap trailing edge at $X/D_m \approx 2.6$ in the large-scale case, whereas in the small-scale case, as the trailing edge is farther downstream, at $X/D = 4$, the same low-frequency wavepackets have higher fluctuation amplitude and thus produce higher-amplitude scattering. This trailing-edge-position effect has been seen in other lab tests, for instance by Amaral et al. (2023). As for the upper range of frequencies, non-jet related sources of aircraft and engine noise may impact the spectral shape in flight test above $St_m = 1$, shaping it differently from the scaled-model tests. On top of the largely broadband spectrum several narrow peaks emerge. Closely-coupled systems may generate marginally extra low-Strouhal broadband noise, but significant additional noise at mid Strouhal numbers $St_m \in [1, 3]$ and emerging tones. Broadband noise trends at low- and at mid-Strouhal ranges are coherent between the academic jet-plate case, the wind-tunnel cases and the flight tests, providing a further justification for the study of canonical jet-plate systems.

2.3 Analysis of Near-Field Surface Pressure Measurements

The wall pressure measurements on realistic geometries are analysed first, and then compared to the findings of academic studies.

2.3.1 Wing Surface Pressure Results from Full- and Large-Scale Tests

Groups of wall-mounted sensors are considered in flight tests and in large-scale wind-tunnel tests. Figure 11 presents results of both tests, where the time history of the fluctuating pressure is plotted against the streamwise position of the sensors. On the left-hand side, the sensors are aligned in the spanwise direction, almost normal to the jet flow. In the center and on the right-hand side, the sensors are aligned with the main direction of the flow.

A prior analysis of near-field wall pressure was conducted to validate the data quality. This analysis focuses on a range of frequencies where jet-flap interaction noise is identified in both the flight tests and wind-tunnel tests. The $St_m = 0.2$ frequency often studied in the literature on jet wavepackets is a very low frequency for the aircraft, sometimes below the audible range, and may sit at the lower bound of the trusted wind-tunnel spectra. Furthermore, with a wing trailing-edge position of the order of $3 \, D_m$ the instability modes at $St_m = 0.2$ are a long way from their peak when they reach the flap trailing edge. The resulting edge diffraction of the modes at this frequency is not as energetic and the noise amplification in the far field not as significant as for frequencies greater than $St_m \approx 0.3$. Both in flight and in wind tunnel, two different engine power settings are used: the idle power where the bypass jet mean velocity is close to flight velocity, and the take-off power where M_s is close to 0.9. The pressure fluctuation levels between take-off power and idle were found to be several orders of magnitude, see Huber et al. (2014) Fig. 10 for near-field pressure spectra in wind tunnel. At take-off, the sensors measured significant fluctuation levels on the range $St_m \in [0.3, 1.4]$. An accentuated flap deflection increased the levels. These main observations are consistent between the aircraft and the reduced-scale models.

Spanwise fluctuations are intense and coherent. The energy peaks at the engine centerline and decreases as sensors are farther away spanwise. In the streamwise direction, fluctuations are correlated over the entire range of streamwise sensors, a distance greater than one jet diameter D_m. We conclude that coherent structures impose their trace from the most upstream all the way to the most downstream microphone located near the flap trailing
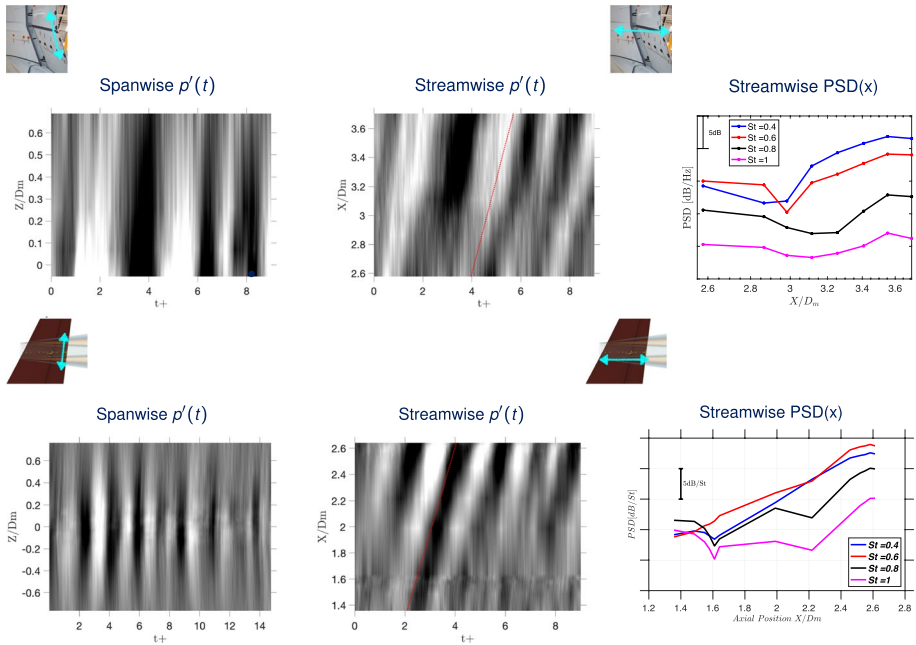
Fig. 11 Unsteady surface pressure measured on the wing pressure side, (top) flight tests and (bottom) in wind tunnel tests. Airbus copyright

edge. The slope provides a convection velocity that is subsonic, much larger than the ambient flight stream velocity and around 0.65 times the fully-mixed jet velocity.

The evolution of power spectral density measured by the surface sensors over the stream-wise direction is also of interest in Fig. 11. On the scaled wing model with pylon, the axial growth ranges between 5 and 15 dB over one D_m pending on the Strouhal number, and is roughly exponential for $St = 0.4$ and $St = 0.6$. Such amplification is qualitatively similar to the growth of instabilities in the local framework, and identified in the case of canonical jets e.g by Breakey (2013). On the aircraft, data on the main wing at $X/D_m \leq 3$ shows roughly constant trends, while steady growth is observed on the flap with amplifications of the order of 2 to 10 dB within 0.7 D_m. Flight-test and reduced scale-test behaviours on the main wing near the gap and on the flap are qualitatively consistent with measured and simulation data on the wing model without pylon presented in Fig. 17, where the significant impact of the wing shape on surface pressure evolution is illustrated. To the authors' knowledge, the observation of the trace of jet coherent structures and their spatial growth on a full-scale aircraft in flight has not been published before.

2.3.2 Comparison of Measurements at the Different Scales

The analysed unsteady pressure fields on the wing lower side are compared to measurements performed on academic single-stream jets and on isolated co-axial nozzle. Figure 12 proposes a summary of this comparison with (a) the isolated nozzle in a laboratory test facility, (b) coaxial nozzle in wind tunnel, (c) installed coaxial nozzle with pylon and wing and (d) the engine in flight test. The complexity of installed nozzle cases (c) and (d) is
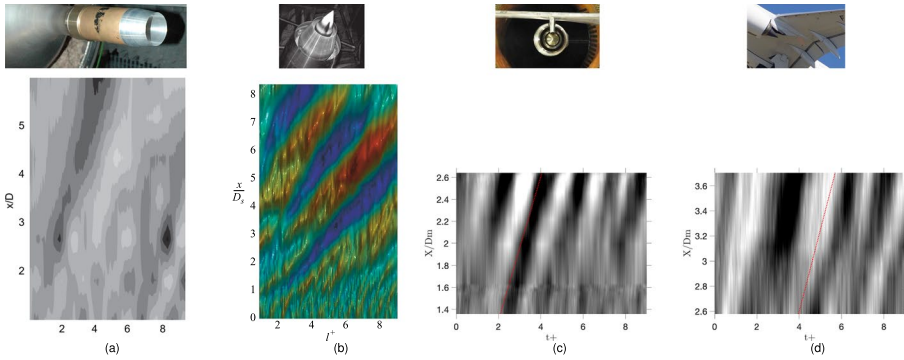
Fig. 12 Jet near-field fluctuating pressure and surface pressure measured at different scales from the laboratory to the aircraft in flight. **a** Data from Breakey et al. (2017), **b** Data from Tinney and Jordan (2008), **c** EXEJET wind-tunnel test data Huber et al. (2014) and **d** A350 flight test data. Airbus copyright

significantly larger with the presence of flight stream, three-dimensional features such as pylon and wing, and Reynolds numbers reaching values around 30 million. Yet the signature of coherent structure is found at all levels of complexity and at all scales. This finding is consistent with two recent reports. The first is a full-scale turbofan engine test at ground where Faranosov et al. (2017) identified a low-order azimuthal structure in the jet sound field due to organized sources. The second is an investigation of jet noise on an aircraft in cruise: Aujogue et al. (2022) showed that near-field acoustic pressure measured on the airplane fuselage was consistent with the shock-associated noise generated by jet wavepackets.

In spite of the large differences between the various test cases, the near-field and wall pressure signatures prove remarkably similar across the tested scales. They indicate that axially-organized structures develop in the mixing layers of installed jet and impose significant pressure fluctuations on the aircraft wing.

Furthermore, it has been shown in wind tunnel by Huber et al. (2014) that unsteady pressures on the lower side and on the upper side of the flap are highly correlated, over a broad spectral range and in flight conditions. This observation substantiates the theory of the linear process of diffraction of the jet near field by the wing.

2.4 Conclusions and Perspectives for Modelling

We conclude that intense, coherent, advecting and exponentially-growing pressure signatures are measured on aircraft wing underside. The jet sources responsible for these signatures diffract at the flap trailing edge. Organized source models have the best chances to reproduce measured signatures and, coupled with a relevant propagator for diffraction, capture jet-airframe interaction noise. This potential appears relevant for the broad variety of cases and scales presented here, from the laboratory nozzle to the aircraft in take-off flight.

3 Methodology

This section describes the methodology chosen and developed to study jet-flap interaction noise. A process is elaborated using a source model and a propagator.

3.1 Source Modelling

The noise source model is chosen to be consistent with organized turbulent structures in the jet. Coherent structures are the product of instability mechanisms triggered on a base flow. Because the isothermal jet is a system that is absolutely stable and convectively unstable Huerre and Monkewitz (1985), our baseline stability analysis is resolved on a spatial domain using Local Stability Analysis (LST) and Parabolized Stability Equations (PSE), and these methods require a base flow.

3.1.1 Base Flow

The FLUSEPA solver is used to generate RANS solutions for the mean flow. FLUSEPA Pont and Brenner (2017) is a solver developed by Arianegroup for launcher propulsion. The turbulence model k-ω with SST-Menter corrections is selected. The mesh includes 13 million cells and relies on the unstructured conservative Chimera capabilities of FLUSEPA.

3.1.2 Stability Analysis

Stability analysis is a theoretical framework that can be used for studying how coherent structures evolve in space and time. Two simplifed approaches are used to predict jet instabilities and form wavepacket source terms: Local Stability Analysis (LST) and non-local analysis by solving Parabolized Stability Equations (PSE). Weakly non-parallel stability analysis via PSE has been shown to predict the average wavepacket and the near pressure field of a mode 0 instability at $St = 0.3$ Jordan et al. (2014). The average wavepacket is not sufficient to produce the sound field of a free jet as the desynchronisation or jitter of wavepackets is a key factor for acoustic efficiency Cavalieri et al. (2011); Cavalieri and Agarwal (2014); Cavalieri et al. (2019). Nogueira et al. (2016a) have shown that this is the case also for jet-plate interaction noise when the plate TE is at four diameters downstream of the nozzle exhaust plane. But when the distance is shortened to three diameters, Faranosov et al. (2019) have obtained absolute noise levels with satisfactory accuracy, suggesting that a perfectly-coherent wavepacket model might be sufficient for noise prediction at small L/D.

The CNRS-ITA PSE solver used in this work is based on developments by Guðmundsson (2010) and Sasaki (2014).

3.1.3 Source Models

Noise generation in free and in installed jets can be modelled using aeroacoustic analogies, provided that the source model is physically relevant. We are therefore interested in modelling the Lighthill's stress tensor. Source terms are directly defined using a single-point formulation, with fluctuations predicted by stability analysis. The selection of source models is composed of a model informed by LST, and a model informed by PSE. Experimental data is required to fill in missing parameters in both models.

Model with Local Stability Data

The case of an isothermal jet of moderate Mach number and at high Reynolds number simplifies the Lighthill's stress tensor by retaining the inertial term and neglecting the viscous term and the entropy fluctuations, to:

$$T_{ij} \approx \rho_0 v_i v_j. \tag{4}$$

Considering that the dominant term of T_{ij} is the product of mean and fluctuating velocities, and that the T_{xx} component dominates the downstream radiation in free field as shown by Cavalieri et al. (2012a), the Fourier transform of Lighthill's tensor can be modelled as

$$T_{ij} \approx T_{11}(y_1, r, \phi, m, \omega) = 2\rho_0 \bar{U}_1(r) u_1'(r, m, \omega) e^{-ik_h(y_1-y_{1c})} e^{-\frac{y_1-y_{1c}^2}{L^2}} e^{im\phi}, \tag{5}$$

where $\bar{U}_1$ is the mean velocity profile at $x = D$ provided by experiments or RANS CFD, and the velocity fluctuations $u_1'(r, m, \omega)$ are modelled as linear instability waves of frequency ω and azimuthal mode m, using LST on the mean velocity profile as a parallel base-flow. The axial wavenumber k_h is also determined using linear stability results. The source is a convected wave enclosed in a Gaussian envelope. y_1 is the axial coordinate and the position of the wavepacket peak amplitude y_{1c} is hypothetized from physical knowledge. The amplitude of u_1' and the length scale L are educed from measurements of the sound field of the free jet, e.g. *from the outside*, following the method proposed by Cavalieri et al. (2012a). Calculation of the radiated sound using Lighthill's acoustic analogy without surface effects led to close agreement between model and experiment for low polar angles.

Model with PSE Data

PSE is now used to provide the velocity fluctuations in an attempt to overcome the high degree of empiricism and hypotheses on source location of the LST approach. Equation 6 illustrates the implementation of a PSE-based source model for T_{11} for given mode and frequency.

$$S_D = T_{11}(y_1, r, \phi, m, \omega) = 2\rho_0 \bar{U}_1(y_1, r) u_1'(y_1, r) e^{im\phi}, \tag{6}$$

where $u_i'(y_1, r) = \hat{u}_i(y_1, r) e^{i \int^{y_1} \alpha(\xi)d\xi}$, product of the slow function in PSE responsible for the amplitude and the rapidly varying part. Note that the kinematic model presented in Eq. 5 may also apply here. In that case, the values of parameters y_{1c}, k_h and L are educed from PSE data and the model is used as a proxy to make PSE solutions radiate.

The PSE provides the velocity fluctuations u_i' with arbitrary amplitude. The amplitude parameter may be obtained either *from the inside* with a hydrodynamic calibration, or *from the outside* using a noise measurement. The PSE-based one-point model is unable to provide absolute levels with hydrodynamic calibration as source de-synchronisation is missing. The exception may be possibly at small L/D around two to three, as suggested in Faranosov et al. (2019), when the non-linear effects on instabilities are still negligible.

3.2 Propagation Modelling

The analysis from wind-tunnel test results shows that we are mostly interested in frequencies $St_m \in [0.3, 3]$. With a wing chord C three times the jet diameter D_m, the frequency range translates into a ratio $C/\lambda_a \in [0.5, 5]$. Additionally, at the subsonic jet Mach numbers around 0.6, the hydrodynamic wavelength is around half the acoustic wavelength, $\lambda_h \simeq \lambda_a/2$. Lift fluctuation noise will occur if $\lambda_h > C$, implying that $C/\lambda_a < 1/2$. Since this value is the lower bound of our interest range, we can expect that the main driver for

jet-flap interaction noise will be diffraction at the trailing edge. For this purpose, several studies such as Nogueira et al. (2016b); Piantanida et al. (2016) and da Silva (2019) have shown that tailored Green's functions (TGF) for the semi-infinite plane can be used to predict the scattered sound field.

Two TGFs have been implemented. The first is the function proposed by Williams and Hall (1970) for a semi-infinite flat plate. This tailored Green's function includes a far-field assumption: observers are located at distances from the edge of many wavelengths. This translates into conditions on kr and r/r_0: $kr \gg 1$ and $r \gg r_0$. This function was adapted to a case with swept trailing edge and used in Piantanida et al. (2016) to study the impact of swept plates. The second is the exact TGF for a semi-infinite flat plate with an ambient flow capability of Roger et al. (2016), for which the first and second gradients of the Green's function with respect to the source coordinates are calculated in Cartesian coordinates.

The applied-mathematics team of Airbus Group has developed the ACTIPOLE software Delnevo et al. (2005); Balin et al. (2016) destined to solve various acoustic propagation problems using integral equations and Boundary-Element Methods (BEM). The main advantages of integral equations and BEM solvers are accuracy and surface meshing. The ACTIPOLE solver includes a fast multipole iterative method to accelerate the resolution. The method will address the diffraction of a perturbation – the convecting wavepacket – by the object. Physically, the BEM mesh represents the finite-chord realistic shape of either plate or wing. this fine representation bears its importance as finite airfoil chord is known to have significant effects on low-frequency trailing-edge noise, see Moreau and Roger (2009).

The coupling between the wavepacket models and the three propagators: either tailored Green's functions and ACTIPOLE, was validated by cross comparing the results between each other, to experimental data as well as to earlier BEM results in Piantanida et al. (2016).

As noted in Piantanida et al. (2016), the analytical TGFs provide a first-order estimate of the jet-plate interaction noise, while the BEM delivers higher precision as it captures secondary lobes and more accurate sound extinctions that are due to other edges and corners. Our industrial modelling objective being to capture the jet wavepacket diffraction by any wing and flap shape, the BEM is selected in the applications in 4.

Assumptions The main assumptions of the overall model are:

- The jet flow is axisymmetric and unaffected by installation. This hypothesis comes the stability analysis method used, and we are able to verify its validity through RANS CFD analysis. The assumption appears however strong for many realistic cases: the pylon and the aircraft wing are both likely to distort the jet into more 3D topologies.
- The ambient flow in which the sound propagates is uniform. This is associated to the TGFs and to the BEM, and is acceptable as long as the flow gradients around realistic configurations are not large.
- Jet blockage and refraction in jet shear layers are negligible. This also comes from the propagation methods and translates into sound wavelengths being an order of magnitude larger than jet diameter, i.e. $St < 1/M_{a,j}$. Such flow-acoustic interaction might occur at low polar angles, where the propagation path of the scattered noise through the jet flow could be of the order of several acoustic wavelengths. This limitation could be overcome by coupling BEM with a finite element method capturing detailed propagation effects through the jet flow.

- The sound diffraction at the jet nozzle is negligible. Indeed, the engine nozzle is not included in our BEM simulations. This assumption seems acceptable given that we study low Strouhal numbers.

4 Evaluation of Model Results Versus Experiments

This section presents the comparison of modelling results against experimental data described in Sect. 2.

4.1 Academic Jet-Plate Cases

The wavepacket model predictions are evaluated against the academic jet-plate configurations. Two source models are applied to a large rectangular plate. In a second step, a more realistic plate design is reproduced by simulation.

4.1.1 Application to the Rectangular Plate

We first compare results of the LST-based model and of the PSE-based model coupled with BEM on the jet diffraction by a rectangular plate as tested in Piantanida et al. (2016). Figure 13 presents results obtained with both models at $St = 0.2$. The choice of $St = 0.2$ is not optimal as we know that PSE performs better at $St \geq 0.3$ Breakey et al. (2017). The Lighthill tensor component T_{11} is modelled with a kinematic source model following Eq. 5. Both models share the same procedure for source amplitude calibration: the amplitude is based on isolated jet measurements in the downstream direction where the axisymmetric mode dominates the sound field. With this calibration on amplitude, the LST-based model recovers the scattered field within 2 dB of the measurements. This is not true for the PSE-based model: the level of empiricism is lower, the parameters are
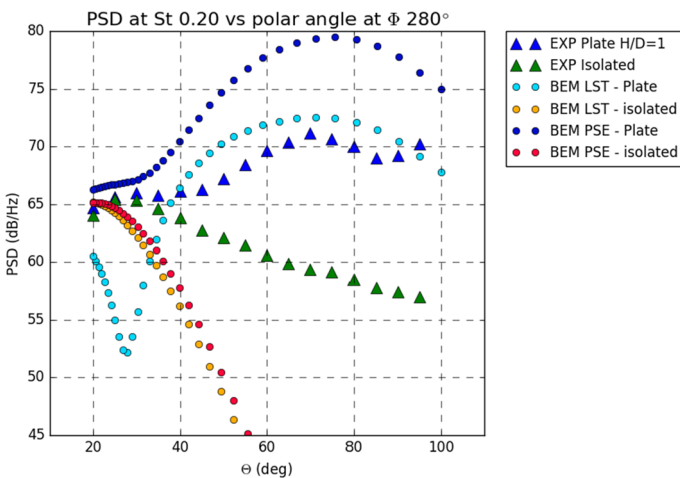

Fig. 13 Noise predictions obtained with LST-based and PSE-based kinematic source models and ACTIPOLE. Experimental data is presented with triangles. Simulation data is shown with dots. The noise source models are calibrated on isolated measurements at $\theta = 20°$. $M_j = 0.6$, St = 0.2, m = 0

not identified from data except for the amplitude, yet its coherence is perfect. In turn its free-field efficiency is unrealistically low, and the calibration on free jet noise leads to an overestimation of the scattered field.

The model with LST and noise eduction is successful at obtaining absolute noise levels and a realistic directivity in the polar direction. This could expected from Cavalieri et al. (2014) and is remarkable considered the large degree of simplification contained in the source model. The eduction of source parameters from free-jet noise allows capturing both direct and scattered sound fields. This confirms that the educed parameters adequately compensate the lack of coherence decay in the model. Note that the match between isolated jet predictions and measurements improves when the azimuthal mode $m = 0$ is extracted from the measured sound field.

With only one parameter informed from data instead of three, the model based on PSE is less empirical than the LST model. The prediction of the polar field shape of installation noise is also satisfactory, however only relative noise levels can be expected from the model. We retain the *PSE-based wavepacket + BEM* prediction scheme to study the impact of plate design.

4.1.2 Application to Different Plate Designs

Piantanida et al. (2016) reported on the significant impact of a swept trailing edge and showed how the other plate edges create additional lobes in the noise field due to secondary diffraction. This experience lead us to design, test and simulate a plate with a realistic wing plan form. Figure 14 show two plates tested at the Bruit et Vent jet laboratory of the PPRIME Institute. The geometries of the rectangular plate and the Wing Plan Form (WPF) plate display a large difference in chord, in trailing-edge axial position ($L/D = 4$ versus 2.67) and in edge sweep angles (0° versus 0° inboard and 18° outboard).

A kinematic wavepacket model was computed based on 2D PSE analysis on the RANS baseflow for the PPRIME single-stream nozzle at $M_j = 0.6$ in static conditions.
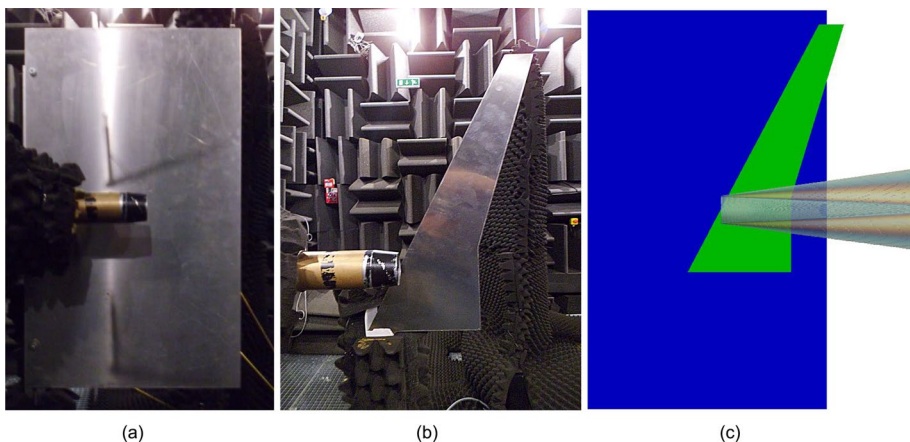

(a)   (b)   (c)

Fig. 14 **a** Rectangular flap plate, **b** Wing Plan Form plate tested at Bruit et Vent, PPRIME, and **c** Shape comparison between the rectangular plate (blue) and the WPF plate (green). Pictures are Airbus and PPRIME copyright
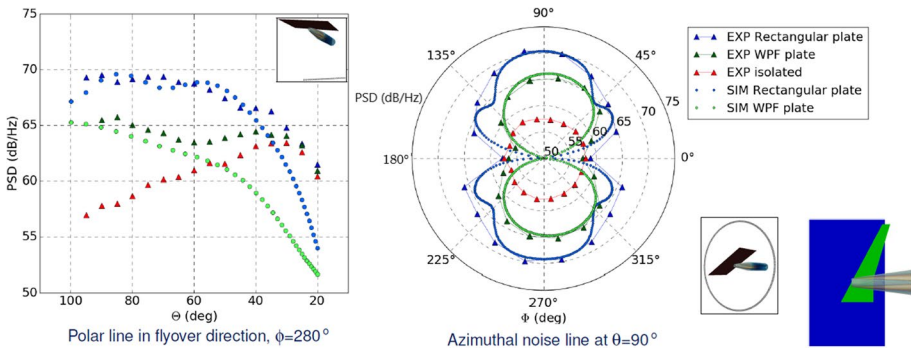
Fig. 15 Noise directivity measured and simulated on two plates: rectangular plate and baseline WPF plate. The source is calibrated on the rectangular plate installed noise peak level. $M_j = 0.6$, St = 0.4, H/D = 1

The BEM solver computed the diffraction of the source on observers at the experimental azimuthal array. Figure 15 presents measured and simulated noise on the two plates, rectangular and WPF.

We first focus on experimental results. An analysis of the microphone noise spectra shows that the effect of WPF plate is visible in the range $St \in [0.1, 1]$, and the magnitude of the effect is maximum at the lower frequency end. Azimuthal and polar directivity indicate marked secondary lobes for the rectangular plate and a single lobe for the WPF plate. As the ratio C/λ is lower for the WPF plate, less secondary lobes are generated. The WPF plate also shifts the peak energy to the inboard sideline. The significant 5 dB noise difference between the realistic WPF and the rectangular plate is believed to originate mainly from the variation in axial distance of the trailing edge: Low-frequency instabilities are in their growth phase as they convect past both plates trailing edges and do not reach its maximum until some diameters downstream, e.g. $X/D = 6$ for $St = 0.4$. Radially-integrated source amplitudes will be lower at $X/D = 2.66$ than at $X/D = 4$, thus the realistic WPF plate is expected to be quieter than the rectangular plate. The partially-swept trailing edge of the realistic WPF redirects the diffraction lobes to the sideline, and, on the account of previous studies involving swept plates Piantanida et al. (2016), might be able to play a role in the lower noise levels in the flyover direction. The impact of trailing-edge partial sweep on wavepacket scattering remains a point to investigate in future work.

The wavepacket-BEM model is able to predict the impact of plate design on noise levels and directivity: Fig. 15 illustrates that the simplified model predicts an accurate noise difference of 5 dB and a correct polar directivity shape in the range of angles where JSI is dominant over free jet noise, i.e. at $\theta > 60°$. The azimuthal directivity shift to $\phi \simeq 310°$ is also well reproduced, and the swept lobe amplitude is captured.

The wavepacket-BEM model is successful at capturing the plate design effect. This achievement enables us to moves forward to realistic wing configurations.

4.2 Realistic Jet-Wing Cases

This section is dedicated to the application of the wavepacket-BEM model to realistic geometries tested in large-scale anechoic wind-tunnel. After a selection of the test cases and the wavepacket model, we mean to identify how the wavepacket-BEM model

captures (1) the near field pressure on the under side of the wing, and (2) a variation of the vertical separation on the acoustic far field.

4.2.1 Selection of the Case and the Prediction Model

Test points are selected from the JERONIMO and AMBROSIA test campaigns with axisymmetric nozzles, at matched-jets $M_j = 0.6$ condition, with the REX80 wing model translated over a range of H/D_m.

The Lighthill's tensor T_{11} is modelled as a kinematic wavepacket using the PSE solution on a single-stream base flow. The $m = 0$ axisymmetric mode is considered, and the model is coupled to ACTIPOLE. The Airbus REX80 wing model is meshed for the BEM solver for frequencies up to $St = 3$.

The wavepacket-BEM prediction model is evaluated against a relevant range of $H/D_m \in [0.8, 1.1]$, for which the jet does not impinge on the flap. Over this range of H/D_m and given the absence of nozzle pylon, the uninstalled jet mean flow hypothesis is close to be satisfied. The domination of JFI noise versus direct jet noise is verified at $H/D_m = 1$ up to $St = 1$ in the forward arc as shown in Figs. 8 and 9.

Simulations have been performed in the Strouhal-number range $St \in [0.2, 1]$ in which JFI noise dominates. The present analysis focuses on $M_j = 0.6$ in static conditions, at two frequencies $St = 0.4$ and $St = 0.8$. At $St = 0.8$, chord and acoustic wavelength are comparable, the ratio $C/\lambda_a = 1.2$, while the chord is larger than the flow scale, $C/\lambda_h = 3.1$.

Figure 16 illustrates the wavepacket diffraction on REX80 wing model at the radial position $H/D_m = 0.8$. Wavefronts in the parallel XZ plane show how the wing is within the hydrodynamic reach, the separation of hydrodynamic and acoustic scales, as well as the upstream propagating wave on the wing suction side. Data in the normal section YZ plane displays the expected extinctions in the spanwise direction, and how the swept trailing edge scatters energy preferentially at a lateral direction toward the wing tip.

4.2.2 Unsteady Surface Pressure

Wall-pressure measurements on sensors located streamwise on the wing model are now reproduced by simulation and results are compared in Fig. 17. Simulated data sets are differentiated between the main wing and the flap, as well as between upper and lower
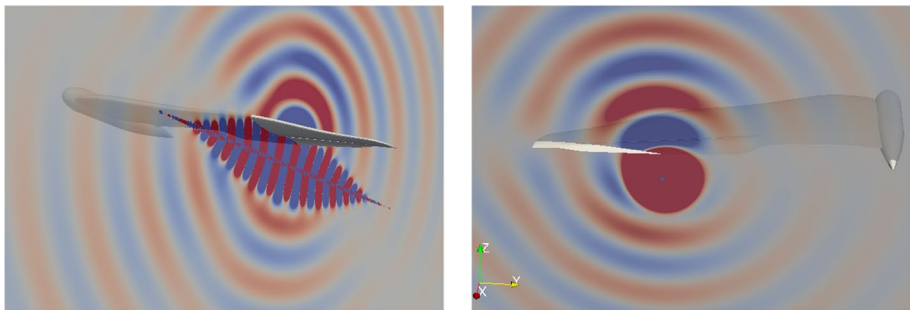

Fig. 16 Real part of pressure on (left) a parallel plane and (right) a normal plane at the flap trailing edge location, computed by ACTIPOLE for the REX80 wing model at position $H/D_m = 0.8$. Kinematic line source wavepacket model, $M_j = 0.6$ in static conditions, $St = 0.8$
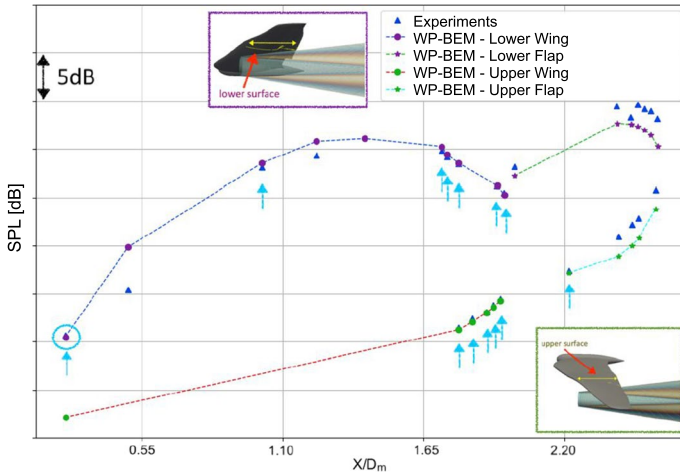
Fig. 17 Sound pressure levels measured and predicted on model-mounted Kulite sensors. Upper and lower side sensors are shown. $M_j = 0.6$ in static conditions, $St = 0.8$, JERONIMO CEPRA19 test

sides. Predictions use a line kinematic wavepacket for the axisymmetric mode of T_{11} and ACTIPOLE at $St = 0.8$, and was calibrated on data measured by the most upstream Kulite sensor located at $X/D_m = 0.2$ and $Y/D_m = 0$, on the lower side, on the jet axis and near the wing leading edge. This calibration can be seen as a kind of initial condition, from which we evaluate if the model can capture the downstream evolution.

Firstly, measurements show that a significant dynamic of 5 to 15 dB separates lower and upper Kulites with higher levels on the lower side. The lower side faces the jet flow which imposes intense hydrodynamic and acoustic fluctuations in its irrotational near field - there surface pressure sensors measure both incident and scattered fields while the upper side measures mainly the scattered field. The shielding of jet hydrodynamic pressure field by the airframe explains the strong level reduction from lower side to upper side. On the lower side, PSD levels increase about exponentially from a position $X/D_m = 0.2$ close to leading edge to $X/D_m = 2.6$ near the trailing edge - a characteristic of jet wavepackets. A 20 dB dynamic was measured between upstream and downstream sensors. Surface curvature is thought to be responsible for the convex shape of the PSD on the wing $X/D_m \in [0.2, 1.8]$.

The T_{11}, $m = 0$ wavepacket-BEM model reproduces well the measured axial PSD evolution on both lower and upper sides of the wing by an order of 1 dB, and on the flap, the gap increases to 2 dB. Because the match is close, each blue arrow indicates when an experimental data point lies below the simulation data. Unfortunately the sensor located on the upper side near the leading edge ($X/D_m = 0.2$) malfunctioned in the test and we could not measure the pressure decay all the way to leading edge. Whereas the source is calibrated against a single point on the wing lower side, the wavepacket-BEM model is able to predict the diffracted field grazing on the surface from the flap trailing edge to the top of main wing at $X/D_m \simeq 1.8$. These results show in particular how the jet wavepacket axisymmetric mode dominates the incident pressure field, and how the BEM predicts an accurate diffraction on the upper wing surface. We now turn our attention to the acoustic field.
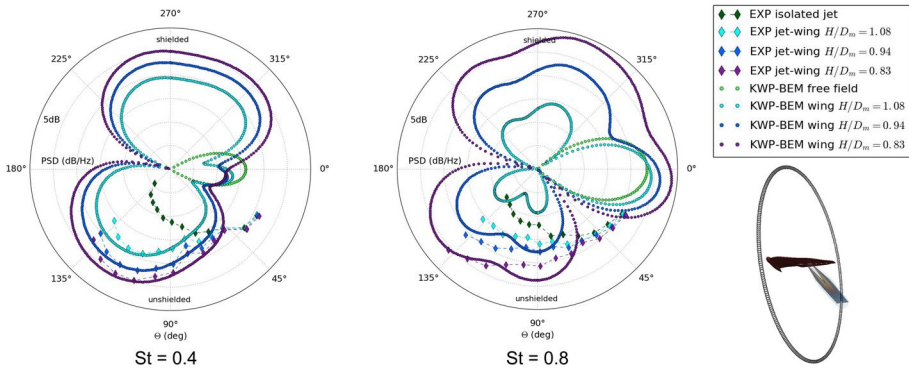
Fig. 18 Noise directivity measured in the AMBROSIA CEPRA19 test and simulated on REX80 wing model. The wavepacket source intensity level is calibrated on the measured noise levels at $[\theta, \phi] = [90°, 270°]$ in the flyover direction. $M_j = 0.6$ in static conditions, and varying H/D_m. AMBROSIA CEPRA19 test campaign. (left) $St = 0.4$ and (right) $St = 0.8$

4.2.3 Acoustic Directivity and Radial Proximity Impact

Three test points are selected from the AMBROSIA CEPRA19 test database to cover the range $H/D_m \in [0.8, 1.1]$. The corresponding free-field noise spectra are displayed in Fig. 8. The analysis now focuses on two frequencies of interest $St = 0.4$ and $St = 0.8$. Figure 18 summarises the results obtained with the T_{11}, $m = 0$ wavepacket-BEM model on a flyover polar arc corresponding to CEPRA19 microphones. For each frequency, a single source is used for all installed cases and its amplitude is calibrated on a single test point and a single microphone: the intermediate configuration corresponding to $H/D_m = 0.94$, and the microphone normal to the nozzle in the flyover direction $[\theta, \phi] = [90, 270]°$. The free-jet measurements and the isolated wavepacket radiation are also presented, however our analysis will focus on the installed wing cases.

At $St = 0.4$ the agreement between experiments and simulation is remarkable: the wavepacket-BEM model predicts the forward directivity of jet-flap interaction noise over almost the entire range of polar angles. The largest disagreement is observed at the most upstream angles ($\theta \sim 135°$) in flyover where sound levels are overestimated by 3 to 4 dB, and where free-field measurements are increasingly difficult to perform.

The wavepacket-BEM model is applied to the same configurations at a higher frequency $St = 0.8$ and calibrated in the same manner as for $St = 0.4$. We bear in mind that at this frequency, jet-flap interaction dominates largely over direct jet noise only for $H/D_m < 1$ and the configuration with the largest radial distance does not exhibit dominant jet-flap interaction noise levels. Figure 18 shows that the model predictions appear globally physical over the range of installed configurations. The model reproduces the measured polar directivity in the flyover direction, within 2 to 3 dB and display a dual-lobe directivity expected at the $C/\lambda_a = 1.2$ ratio. The dual-lobe feature is present in the experimental data but in a much more subtle manner at flyover than in the simulation.

5 Conclusion

We combined an analysis of experimental data and simplified noise source and propagation modelling to improve the understanding and the prediction of broadband jet-flap interaction noise.

Jet-flap interaction is characterized over a wide range of test scales: laboratory canonical configurations, realistic large-scale wind tunnel, and full-scale aircraft in flight. Broadband JFI tends to dominate jet noise at low Strouhal-number range [0.3, 1.5] and at forward polar angles $\theta \geq 90°$. On top of the broadband spectrum, narrow-band peaks are believed to be signatures of tonal-jet flap interaction Jordan et al. (2018).

Coherent, advecting and exponentially-growing surface pressure signatures are discovered not only at reduced model scale but also on an aircraft wing in flight. One-fiftieth laboratory jets, one-tenth scale wind-tunnel jets and full-scale engine jets generate similar signatures in the near field: axially-organized structures impose significant pressure fluctuations on the wing. The data analysis confirms the choice of wavepacket models to describe this observed behaviour, and substantiates the hypothesis that the flap edge discontinuity radiates sound due to diffraction of organized structures.

A methodology is developed to predict jet-flap interaction noise based on wavepacket source models, and includes base flow estimation with RANS CFD, stability analysis, noise source and propagation modelling. In our studied cases the surface trailing edge is positioned upstream of the jet potential core, this provides an opportunity to use linear stability theory for noise source modelling. Beyond the end of the potential core, modelling with linear-stability tools becomes more complex due to the non-modal nature of wavepacket dynamics. While the empirical wavepacket based on LST and noise eduction is found to be relevant to study the phenomenon, non-local one-dimensional PSE is selected for its robustness and its account of a slowly varying jet. A key assumption is the mean flow axisymmetry, i.e. the sources are unaffected by installation. The noise source models use the information from stability analysis: A kinematic one-point model is used as a proxy to make PSE results radiate sound. The PSE directly provides values for all parameters except for the amplitude that remains to be calibrated using acoustic data on a single installed measurement. The source model is chained to propagators able to capture the wavepacket diffraction by surfaces. The analytical tailored Green's function provides a first-order estimate of the scattered sound field, while the BEM delivers results at higher precision.

Physical effects are studied with the low-order modelling strategy: airframe design and engine positioning under wing. First, a flat plate with realistic wing plan form and a short chord was tested, combining the two physical effects of trailing-edge sweep and of chord length on wavepacket diffraction. The wavepacket-BEM model is able to predict the reduced and relocated diffraction lobes due to the plate design. Then, the wavepacket-BEM model is applied to realistic exhaust-airframe configurations. Unsteady surface pressure fluctuations are examined on a realistic wing and flap at $H/D_m = 0.8$. Simulation results compared to surface sensors measurements show that the T_{11}, $m = 0$ kinematic wavepacket model coupled to ACTIPOLE predicts a correct pressure amplification rate from wing leading edge to flap trailing edge and accurate diffraction on the upper surface. The acoustic directivity of JFI matches well at low frequencies $St = 0.4$ but could be improved at $St = 0.8$. The JFI noise amplification measured with decreasing H/D_m from 1.1 to 0.8 is captured with higher accuracy at $St = 0.4$ than at $St = 0.8$. Future investigations should explain the remaining discrepancies at higher frequency, and study the azimuthal directivity.

Although the degree of simplification of the turbulent jet as a noise source is considerable, the model could reproduce jet-flap interaction trends measured on canonical jet-plate cases as well as on realistic geometries. Consistently with previous work at academic level Cavalieri et al. (2014); Piantanida et al. (2016); Nogueira et al. (2016); da Silva (2019), the axisymmetric mode is identified on both academic and realistic test cases as the dominant component of the jet hydrodynamic near-field pressure, and the most efficient source of JFI noise. Our results corroborate the choice of T_{11} to obtain jet installation noise characteristics at the first order.

Our results support the contention that the coherent structures generated by the Kelvin-Helmholtz instability of the turbulent mean field are the main sources of jet-airframe interaction noise through a diffraction process, this not only in the jet laboratory but also in large-scale wind tunnel and for a full-scale aircraft with 30-million Reynolds-number engine jet flows.

A first perspective to this work is to apply the wavepacket-BEM methodology to jets in flight and compare the results to CEPRA19 wind-on measurements. The present model contains all the necessary ingredients for such study, and the method appears all the more promising on the account of the flight-effect analysis by Bychkov et al.[35]. Modern engine installation creates complex flows, both the engine pylon and the high-lifting wing are likely to distort the jet. To investigate such installed jets in flight conditions, the modelling strategy should be upgraded with three-dimensional PSE Avanci et al. (2022). Another direction is the Resolvent analysis which has the capability to remove some empiricism on the predicted wavepacket amplitude and coherence. The resolvent framework should then be combined with a model for the forcing that correctly reproduces the sound-producing wavepackets Karban et al. (2022).

Author Contributions JH performed the modelling, the stability and aeroacoustic simulations and the data analysis. GP performed the RANS CFD and provided support on data processing. PJ provided the PSE solver. MR provided the tailored Green's function with flow. JH, PJ and MR discussed the data interpretation. JH wrote the manuscript. All the authors read and approved the final version of the manuscript.

Declarations

Conflict of interest The authors report no competing interests that might be perceived to influence the results and/or discussion reported in this paper.

Ethics approval Not applicable.

Informed consent Not applicable.

References

Amaral, F.R., Lebedev, A., Jordan, P.: Experiments on installed jet noise. In: AIAA Aviation 2023 Forum. https://doi.org/10.2514/6.2023-3830

Aujogue, N., Huber, J., Julliard, E., Antoni, J., Leclère, Q.: Experimental investigation of the supersonic jet noise from aircraft engines using acoustic imaging. In: 28th AIAA/CEAS Aeroacoustics 2022 Conference. https://doi.org/10.2514/6.2022-2867

Avanci, M.P., Robinet, J.-C., Jordan, P., Huber, J., Pont, G.: Application of 3D-parabolized stability equations to asymmetric jets. In: 28th AIAA/CEAS Aeroacoustics 2022 Conference (2022)

Balin, N., Sylvand, G., Robert, J.: Fast methods applied to BEM solvers for acoustic propagation problems. In: 22nd AIAA/CEAS Aeroacoustics Conference. AIAA 2016-2712, Lyon, France (2016)

Belyaev, I.V., Zaytsev, M.Y., Kopiev, V.F., Ostrikov, N.N., Faranosov, G.A.: Studying the effect of flap angle on the noise of interaction of a high-bypass jet with a swept wing in a co-flow. Acoust. Phys. **63**, 14–25 (2017). https://doi.org/10.1134/S1063771016060026

Blandeau, V., Regnier, V., Bousquet, P.: Acoustic behaviour of ground plates for aircraft noise flight tests. In: 24th AIAA/CEAS Aeroacoustics Conference, pp. 2018–3295 (2018)

Blandeau, V.P., Bousquet, P.: A new plate design to improve the accuracy of aircraft exterior noise measurements on the ground. In: AIAA Aviation 2021 Forum, pp. 2021–2158 (2021)

Blandeau, V.P., Bousquet, P., Bennani, A., Chaigne, B., Abboud, T.: Aircraft noise measurement with ground microphones: Effects of noise propagation around and under the reflective plate edges. In: AIAA AVIATION 2023 Forum, p. 4165 (2023)

Boeing: Low-speed Aeroacoustic Facility. http://www.boeing.com/commercial/techsvcs/boeingtech/bts_acoub.html

Breakey, D.E.S., Jordan, P., Cavalieri, A.V.G., Léon, O., Zhang, M., Lehnasch, G., Colonius, T., Rodríguez, D.: Near-field wavepackets and the far-field sound of a subsonic jet. In: 19th AIAA / CEAS Aeroacoustics Conference, Berlin, Germany (2013)

Breakey, D.E.S., Jordan, P., Cavalieri, A.V.G., Nogueira, P.A.S., Léon, O., Colonius, T., Rodríguez, D.: Experimental study of turbulent-jet wave packets and their acoustic efficiency. Phys. Rev. Fluids **2**(124601) (2017)

Brown, W.H., Ahuja, K.K.: Jet and wing/flap interaction noise. In: 9th AIAA/CEAS Aeroacoustics Conference (1984)

Bushell, K.W.: Measurement and prediction of jet noise in flight. In: AIAA 2nd Aeroacoustics Conference, Hampton, VA, USA (1975)

Bychkov, O.P., Faranosov, G.A.: On the possible mechanism of the jet noise intensification near a wing. Acoust. Phys. **60**(6), 633–646 (2014). https://doi.org/10.1134/S1063771014060050

Bychkov, O.P., Faranosov, G.A.: An experimental study and theoretical simulation of jet-wing interaction noise. Acoust. Phys. **64**(4), 437–452 (2018). https://doi.org/10.1134/S1063771018030041

Bychkov, O., Faranosov, G., Kopiev, V., Soares, L.F.M., Cavalieri, A.V.G.: Jet installation noise modeling in static and flight conditions using centerline fluctuations. AIAA J. **60**(6), 3620–3634 (2022). https://doi.org/10.2514/1.J060879

Cavalieri, A.V.G., Agarwal, A.: Coherence decay and its impact on sound radiation by wavepackets. J. Fluid Mech. **748**, 399–415 (2014)

Cavalieri, A.V.G., Jordan, P., Agarwal, A., Gervais, Y.: Jittering wave-packet models for subsonic jet noise. J. Sound Vib. **330**(18), 4474–4492 (2011)

Cavalieri, A.V.G., Jordan, P., Colonius, T., Gervais, Y.: Axisymmetric superdirectivity in subsonic jets. J. Fluid Mech. **704**, 388 (2012a)

Cavalieri, A., Jordan, P., Gervais, Y., *et al.*: Scattering of wavepackets by a flat plate in the vicinity of a turbulent jet. In: 18th AIAA/CEAS Aeroacoustics Conference, Colorado Springs, CO, USA (2012b)

Cavalieri, A.V.G., Jordan, P., Lesshafft, L.: Wave-packet models for jet dynamics and sound radiation. Appl. Mech. Rev. **71**(2), 020802 (2019)

Cavalieri, A.V.G., Jordan, P., Wolf, W., Gervais, Y.: Scattering of wavepackets by a flat plate in the vicinity of a turbulent jet. J. Sound Vib. **333**(24), 6516–31 (2014)

da Silva, F.D., Jordan, P., Cavalieri, A.V.G.: On the modeling of wavepacket scattering noise with coherence effects. J. Acoust. Soc. Am. **146**(6), 4472–4480 (2019)

David, F., Jourdan, J.-M., Cléro, F., Koenig, M., Huber, J.: Large-scale jet noise testing, reduction and methods validation EXEJET: 4. flows characterization with PIV in the CEPRA19 anechoic wind tunnel of ONERA. In: 20th AIAA/CEAS Aeroacoustics Conference, Atlanta, GA, USA (2014)

Davy, R., Brossard, C., Jourdan, J.-M., Pioche, Y., Piccin, O.: Installation effects characterization of VHBR engines: 2. experimental study using particle image velocimetry. In: 15th AIAA/CEAS Aeroacoustics Conference, Miami, FL (2009)

Dawson, M., Lawrence, J., Self, R., Kingan, M.: Validation of a jet-surface interaction noise model in flight. AIAA J. **58**(3), 1130–1139 (2020)

Delnevo, A., Le Saint, S., Sylvand, G., Terrasse, I.: Numerical methods - fast multipole method for shielding effects. In: 10th AIAA/CEAS Aeroacoustics Conference. AIAA 2005-2971, Seattle, WA, USA (2005)

Dezitter, F., Bezard, H., de Saint Victor, X., Zeggai, K., Britchford, K., Joubert, G., Puigt, G.: Installation effects characterization of VHBR engines: 3. CFD assessment for jet mixing. In: 15th AIAA/CEAS Aeroacoustics Conference, Miami FL (2009)

Elkoby, R.: Full-scale propulsion airframe aeroacoustics investigation. In: 11th AIAA/CEAS Aeroacoustics Conference, Monterey CA, USA (2005)

Faranosov, G.A., Belyaev, I.V., Kopiev, V.F., Zaytsev, M.Y., Aleksentsev, A.A., Bersenev, Y.V., Chursin, V.A., Viskova, T.A.: Adaptation of the azimuthal decomposition technique to jet noise measurements in full-scale tests. AIAA J. **55**(2), 572–584 (2017). https://doi.org/10.2514/1.J055001

Faranosov, G., Bychkov, O.P., Kopiev, V., Soares, L.F., Cavalieri, A.V.: The Modeling of Jet-Plate Interaction Noise in the Presence of Co-Flow. In: 25th AIAA/CEAS Aeroacoustics Conference, Delft, The Netherlands (2019). https://doi.org/10.2514/6.2019-2492

Fleury, V., Bulté, J.: Extension of deconvolution algorithms for the mapping of moving acoustic sources. J. Acoust. Soc. Am. **129**(3), 1417–1428 (2011)

Fleury, V., Davy, R.: Large-scale jet noise testing, reduction and methods validation EXEJET: 5. analysis of jet-airfoil interaction noise by microphone array techniques. In: 20th AIAA/CEAS Aeroacoustics Conference, Atlanta, GA, USA (2014)

Guðmundsson, K.: Instability wave models of turbulent jets from round and serrated nozzles. PhD thesis, California Institute of Technology (2010)

Head, R.W., Fisher, M.J.: Jet/surface interaction noise: analysis of far-field low-frequency augmentation of jet noise due to the presence of a solid shield. In: 3rd Aeroacoustics Conference (1976)

Huber, J., Omais, M., Vuillemin, A., Davy, R.: Characterization of installation effets for HBPR engine part IV: Assessment of jet acoustics. In: 15th AIAA/CEAS Aeroacoustics Conference, Miami FL, USA (2009)

Huber, J., Drochon, G., Pintado-Peno, A., Cléro, F., Bodard, G.: Large-scale jet noise testing, reduction and methods validation EXEJET: 1. project overview and focus on installation. In: 20th AIAA/CEAS Aeroacoustics Conference, Atlanta, GA, USA (2014)

Huerre, P., Monkewitz, P.: Absolute and convective instabilities in free shear layers. J. Fluid Mech. **159**, 151–168 (1985)

Jordan, P., Colonius, T., Brès, G., Zhang, M., Towne, A., Lele, S.K.: Modeling intermittent wavepackets and their radiated sound in a turbulent jet. In: Proceedings of the CTR Summer Program 2014, Stanford, CA, USA (2014)

Jordan, P., Jaunet, V., Towne, A., Cavalieri, A.V.G., Colonius, T., Schmidt, O., Agarwal, A.: Jet-flap interaction tones. J. Fluid Mech. **853**, 333–358 (2018). https://doi.org/10.1017/jfm.2018.566

Karban, U., Bugeat, B., Agarwal, A., Lesshafft, L., Jordan, P.: An empirical model of noise sources in subsonic jets, formulated in a linear resolvent framework. In: 28th AIAA/CEAS Aeroacoustics 2022 Conference (2022)

Lawrence, J.L.T.: Aeroacoustic interactions of installed subsonic round jets. PhD thesis, University of Southampton, Institute of Sound and Vibration Research (2014)

Leiba, R., Demontis, H., Leclere, Q., Fouqueux, S., Julliard, E.: Acoustic imaging on aircraft flyover tests: Comparing CLEAN-T to DAMAS-MS. In: 10th Convention of the European Acoustics Association, Forum Acusticum (2023)

Léon, O., Brazier, J.-P.: Investigation of the near and far pressure fields of dual-stream jets using an Euler-based PSE model. In: 19th AIAA/CEAS Aeroacoustics Conference, Berlin, Germany (2013). https://doi.org/10.2514/6.2013-2280

Low, J.K.C.: Effects of forward motion on jet and core noise. In: AIAA 4th Aeroacoustics Conference, Atlanta, Georgia, USA (1977)

Lyu, B., Dowling, A.P.: On the mechanism and reduction of installed jet noise. In: 23rd AIAA/CEAS Aeroacoustics Conference, Denver, CO, USA (2017)

Lyu, B., Dowling, A.P.: Modelling installed jet noise due to the scattering of jet instability waves by swept wings. J. Fluid Mech. **870**, 760–783 (2019). https://doi.org/10.1017/jfm.2019.268

Lyu, B., Dowling, A.P., Naqvi, I.: Prediction of installed jet noise. J. Fluid Mech. **811**, 234–268 (2017)

Mead, C.J., Strange, P.J.R.: Under-wing installation effects on jet noise at sideline. In: 4th AIAA/CEAS Aeroacoustics Conference (1998)

Meloni, S., Mancinelli, M., Camussi, R., Huber, J.: Wall pressure fluctuations induced by a compressible jet in installed configuration. AIAA J. **58**(7), 2991–3000 (2020)

Mengle, V.G.: The effect of nozzle-to-wing gulley height on jet flow attachment to the wing and jet-flap interaction noise. In: 17th AIAA/CEAS Aeroacoustics Conference, Portland, OR, USA (2011)

Mengle, V.G., Elkoby, R., Brusniak, L., Thomas, R.H.: Reducing propulsion airframe aeroacoustic interactions with uniquely tailored chevrons: 2. installed nozzles. In: 12th AIAA/CEAS Aeroacoustics Conference, Cambridge, MA (2006a)

Mengle, V.G., Elkoby, R., Brusniak, L., Thomas, R.: Reducing propulsion airframe aeroacoustic interactions with uniquely tailored chevrons: 3. jet-flap interaction. In: 12th AIAA/CEAS Aeroacoustics Conference, Cambridge, MA (2006b)

Mengle, V.G., Stoker, R.W., Brusniak, L., ans R. H. Thomas, R.E.: Flaperon modification effect on jet-flap interaction noise reduction for chevron nozzles. In: 13th AIAA/CEAS Aeroacoustics Conference, Roma, Italy (2007)

Miller, W.R.: Flight effects for jet-airframe interaction noise. In: 8th AIAA Aeroacoustics Conference. AIAA-1983-0784, Atlanta, Georgia, USA (1983)

Moreau, S., Roger, M.: Back-scattering correction and further extensions of Amiet's trailing-edge noise model. Part ii: Application. J. Sound Vib. **323**(1), 397–425 (2009). https://doi.org/10.1016/j.jsv.2008.11.051

Nogueira, P.A.S., Cavalieri, A.V.G., Jordan, P.: A model problem for sound radiation by an installed jet. J. Sound Vib. **391**, 95–115 (2016a)

Nogueira, P.A.S., Piantanida, S., Cavalieri, A.V.G., Jordan, P.: PSE-based prediction of sound radiation by installed jets. In: 22nd AIAA/CEAS Aeroacoustics Conference, Lyon, France (2016b)

Perrino, M.: An experimental study into pylon, wing, and flap installation effects on jet noise generated by commercial aircraft. PhD thesis (2014)

Piantanida, S., Jaunet, V., Huber, J., Wolf, W.R., Jordan, P., Cavalieri, A.V.G.: Scattering of turbulent-jet wavepackets by a swept trailing edge. J. Acoust. Soc. Am. **140**(6), 4350 (2016). https://doi.org/10.1121/1.4971425

Piantanida, S.: Time and frequency domain modelling of turbulent-jet wavepackets for free and installed jet noise. PhD thesis, Université de Poitiers (2017)

Piccin, O.: CEPRA19: the ONERA large anechoic facility. In: 15th AIAA/CEAS Aeroacoustics Conference, Miami, FL (2009)

Pont, G., Brenner, P.: High order finite volume scheme and conservative grid overlapping technique for complex industrial applications. In: International Conference on Finite Volumes for Complex Applications, pp. 295–303 (2017). https://doi.org/10.1007/978-3-319-57394-6_32

Reddy, N.N., Tanna, H.K.: Installation effects on jet noise in flight. In: 6th Aeroacoustics Conference (1980). https://doi.org/10.2514/6.1980-1044

Roger, M., Moreau, S., Kucukcoskun, K.: On sound scattering by rigid edges and wedges in a flow, with applications to high-lift device aeroacoustics. J. Sound Vib. **362**, 252–275 (2016)

Rolls-Royce Ltd.: Trent XWB. https://www.rolls-royce.com/products-and-services/civil-aerospace/airlines/trent-xwb.aspx#section-overview

Sasaki, K.: Estudo de controle de pacotes de onda em jatos utilizando as equacoes de estabilidade parabolizadas. Master's thesis, Instituto Tecnologico de Aeronautica, Sao Jose Dos Campos, SP - Brazil (2014)

SenGupta, G.: Analysis of jet-airframe interaction noise. In: 8th Aeroacoustics Conference (1983)

Shearin, J.G.: Investigation of jet-installation noise sources under static conditions. NASA-TP-2181, NASA, Langley Research Center; Hampton, VA, United States (1983)

Shivashankara, B.N., Blackner, A.M.: Installed jet noise. In: 3rd AIAA/CEAS Aeroacoustics Conference (1997)

Southern, I.S.: Exhaust noise in flight: the role of acoustic installation effects. In: 6th AIAA Aeroacoustics Conference (1980)

Tinney, C.E., Jordan, P.: The near pressure field of co-axial subsonic jets. J. Fluid Mech. **611**, 175–204 (2008)

Viswanathan, K.: Does a model-scale nozzle emit the same jet noise as a jet engine? AIAA J. **46**(2), 336–355 (2008). https://doi.org/10.2514/1.18019

Viswanathan, K.: Best practices for accurate measurement of pure jet noise. Int. J. Aeroacoust. **9**(1), 145–206 (2010)

Wang, M.: Wing effect on jet noise propagation. In: 6th AIAA Aeroacoustics Conference (1980)

Way, D.J., Turner, B.A.: Model tests demonstrating under-wing installations effects on engine exhaust noise. In: 6th AIAA Aeroacoustics Conference (1980)

Williams, J.E.F., Hall, L.H.: Aerodynamic sound generation by turbulent flow in the vicinity of a scattering half plane. J. Fluid Mech. **40**(4), 657–670 (1970)

Authors and Affiliations

Jérôme Huber[1] · Grégoire Pont[2] · Peter Jordan[3] · Michel Roger[4]

✉ Jérôme Huber
jerome.huber@airbus.com

Grégoire Pont
gregoire.pont@airbus.com

Peter Jordan
peter.jordan@univ-poitiers.fr

Michel Roger
michel.roger@ec-lyon.fr

[1] Aeroacoustic Sources, Airbus Operations SAS, Toulouse, France

[2] Modelling and Simulation, Airbus, Toulouse, France

[3] PPRIME Intitute, Université de Poitiers, Chasseneuil du Poitou, France

[4] Centre Acoustique, École Centrale de Lyon, Ecully, France